Superconductivity in Borides

Anooja Jayaraj

A dissertation submitted for the partial fulfilment of

BS-MS dual degree in Science

Indian Institute of Science Education and Research Mohali

April 2016

Certificate of Examination

This is to certify that the dissertation titled “Superconductivity in Borides” submitted by Ms. Anooja Jayaraj (Reg. No. MS11031) for the partial fulfilment of BS-MS dual degree programme of the Institute, has been examined by the thesis committee duly appointed by the Institute. The committee finds the work done by the candidate satisfactory and recommends that the report be accepted.

Dr. Sanjeev Kumar Dr. Goutam Sheet Dr. Yogesh Singh

(Supervisor)

Dated: April 21, 2016

Declaration

The work presented in this dissertation has been carried out by me under the guidance of Dr. Yogesh Singh at the Indian Institute of Science Education and Research Mohali.

This work has not been submitted in part or in full for a degree, a diploma, or a fellowship to any other university or institute. Whenever contributions of others are involved, every effort is made to indicate this clearly, with due acknowledgement of collaborative research and discussions. This thesis is a bonafide record of original work done by me and all sources listed within have been detailed in the bibliography.

Anooja Jayaraj

(Candidate)

Dated: April 21, 2016

In my capacity as the supervisor of the candidate's project work, I certify that the above statements by the candidate are true to the best of my knowledge.

Dr. Yogesh Singh

(Supervisor)

Acknowledgement

I would like to thank my supervisor Dr. Yogesh Singh for his guidance and support during my project. I had a wonderful time working in his lab. A special thanks goes to Jaskaran for helping me throughout the project and for being the coolest person I have ever seen. I am also deeply indebted to the members of the Novel Materials Lab: Gyaneshwar sir for helping me with XRD refinements (he makes refinement look like it is so simple), Anzar, Amit, Kavita and Ashwini for helping me with various measurements and for being such nice people.

I am grateful to my friends here at IISER Mohali who made this place a home away from home. I am thankful to Tess for being with me from the beginning, and patiently bearing me during all my moods, both good and bad. A shout out to Anjali for her awesomeness, all the fun we had in our final year and for teaching me that it is okay to be crazy sometimes. I am also thankful to Vivek for being such a great friend in every way even though we irritate each other so much. I am thankful to Thapasya for the memories we share.

No words will ever suffice to express my gratitude to my parents and sister. They have been my support system through all these years and continue to encourage me and trust me from so far away.

List of Figures

List of Tables

Contents

Dedicated to my parents and sister

Abstract

The discovery of a novel superconducting state in MgB_2 has led to an interest in borides. We have studied several boride compounds to gain greater insight into this new phenomenon. Polycrystalline samples of OsB_2 and RuB_2 were grown in a tetra arc furnace. X-Ray Diffraction (XRD) data shows that OsB_2 crystallizes in orthorhombic structure at room temperature. They contain alternate boron and osmium layers stacked along c-axis. The boron layers in MgB_2 are flat whereas that in OsB_2 has a chair-like structure. Electrical resistivity measurements were carried out to study superconducting properties of OsB_2. It was observed that OsB_2 becomes superconducting below $T_c = 2.1$ K. The resistivity measurement of RuB_2 shows that it becomes superconducting below 1.6 K. $LuRuB_2$ was found to be superconducting at around 10.98 K. Pressure studies on the sample showed that the critical temperature decreases with increasing pressure.

Chapter 1

Introduction

1.1 Superconductivity

Superconductivity is a phenomenon in which certain materials show zero electrical resistance and expulsion of magnetic field when they are cooled below a characteristic critical temperature (often denoted as T_c). Superconductors are often defined by three important parameters:

T_c - The highest temperature at which superconductivity occurs in a material. Below this transition temperature T_c, the resistivity of the material is equal to zero.

H_c - Above this value of an externally applied magnetic field a superconductor becomes non superconducting.

I_c - The maximum value of electrical current that a superconductor can carry without resistance. The existence of a critical field dictates that there will be a critical current. As current flows through a wire, it creates a magnetic field. When the field due to the current becomes equal to H_c, superconductivity is destroyed.

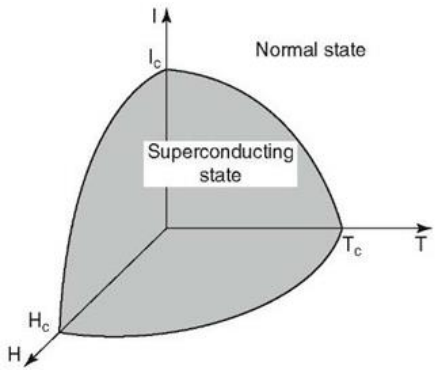

Figure 1.1 The limits of superconductivity are defined in this critical T-H-I-diagram. | Source: http://what-when-how.com/electronic-properties-of-materials/electrical-conduction-in-metals-and-alloys-electrical-properties-of-materials-part-2/ |

1.2 Meissner Effect

The expulsion of magnetic field from the interior of a superconductor is called Meissner Effect. It is this effect which makes superconductors different from perfect conductors which would also ideally show zero resistance. Meissner effect is due to electric currents called screening currents which flow on the surface of the superconductor generating a field equal and opposite to the applied field. Meissner effect is responsible for the existence of critical field H_c. The energy stored in the field per unit volume is greater for Meissner state when compared to the normal state in which field penetrates the sample uniformly. As magnetic field is increased, the increased field energy exceeds the energy difference between normal and superconducting states. Thus the superconducting sample reverts to its normal state.

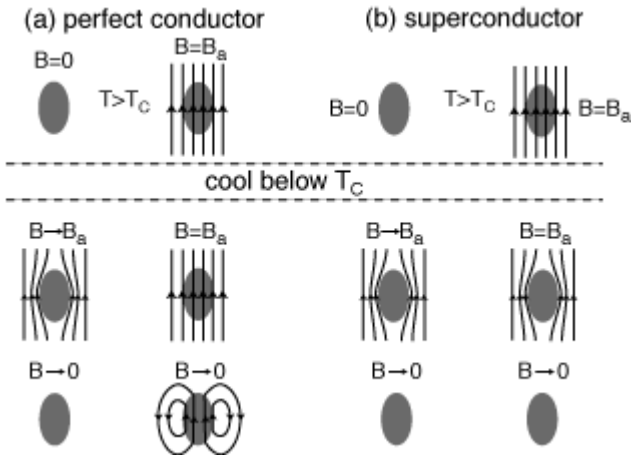

Figure 1.2 A comparison of superconductor and perfect conductor shows that the field inside a superconductor is zero below T_c independent of sample history. | Source: http://users-phys.au.dk/philip/pictures/solid_superconductivity/meissner.gif |

1.3 Theory of Superconductivity

A theory that was quite successful in explaining superconductivity was the BCS theory. This theory predicts the existence of an energy gap Δ separating the states of superconducting electrons and normal electrons. The reason for this energy gap is due to binding of superconducting electrons into Cooper pairs. Thus energy equal to 2Δ has to be provided to break the Cooper pair. The attractive interaction between otherwise repelling electrons is due to lattice vibrations. An electron attracts the positive ions in the lattice as it moves through a metal. This gives rise to an increased positive charge density as shown in Figure 1.2. The ions, being much larger and heavier, move slower than the electrons. So the enhanced charged density remains after the electron has passed and can attract another electron. So the attraction between the two electrons is said to be due to the exchange of a virtual phonon.

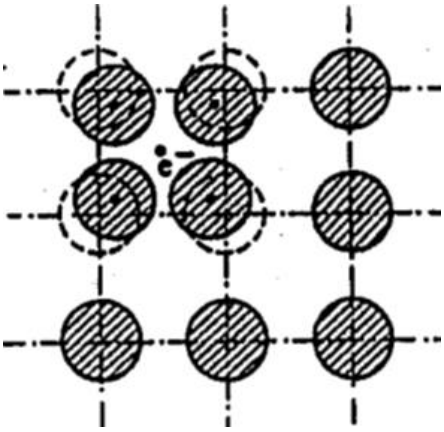

Figure 1.3 An electron polarizing positive ions in its vicinity to create an attractive potential for a following second electron | Source: Solid State Physics, Part IV, Superconducting Properties of Solids, M. S. Dresselhaus |

Some of the basic BCS results include

- All the electrons in a superconductor can be described by a single quantum mechanical wave function $\Psi(r)$.
- The electrons are bound in pairs and have opposite spins and momentum.
- They are bound by an energy Δ_0 and the energy gap is given by $E_g \approx 3.5k_BT_c$.

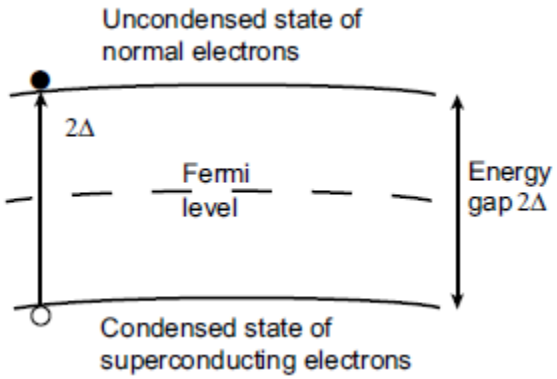

Figure 1.4 The energy gap between normal and superconducting electrons as predicted by the BCS theory

The characteristic behavior of superconductors could be explained by the London equation which shows that the currents responsible for screening of magnetic field should be described by

$$\nabla \times j = \frac{-n_s e^2 \boldsymbol{B}}{m} \quad (1)$$

Here j is current, n_s is the number of superconducting electrons, **B** is the magnetic field and e and m are charge and mass of an electron. We also have the Maxwell's equations

$$\nabla \times \boldsymbol{B} = \mu_0 \boldsymbol{j} \quad (2)$$

$$\nabla . \boldsymbol{B} = 0 \quad (3)$$

Combining equations (1), (2) and (3) we get that the field **B** inside a superconductor satisfies

$$\lambda^2 \nabla^2 \boldsymbol{B} = \boldsymbol{B} \quad (4)$$

where $\lambda^2 = m/\mu_0 n_s e^2$. The solution for equation (4) is given by

$$B(x) = B_0 e^{\frac{-x}{\lambda}} \quad (5)$$

Thus, the magnetic field decays exponentially with distance into the superconductor with a characteristic length scale λ, called the penetration depth. The penetration depth is about 1700 nm, which means that magnetic field is effectively excluded from the interior of macroscopic samples. Another important length scale in superconductors is the coherence length ξ. It is the average distance between the electrons in a Cooper pair and is given by

$$\xi = \hbar v_F / \pi \Delta \quad (6)$$

where v_F is the velocity of electrons in the Fermi surface and Δ is the energy band gap. A parameter κ, defined as the ratio λ/ξ is used to differentiate between the different types of superconductors, which have been described in the following section.

1.4 Thermodynamics of Superconducting Transition

The critical field at which the normal and superconducting states are in equilibrium can be found by equating the Gibbs free energy in each state. It has been found to be given by the following equation

$$G_N(0,T) - G_S(0,T) = \frac{B_c^2}{2\mu_0} \quad (7)$$

where G_N and G_S are the Gibbs free energy in the normal and superconducting states and B_c is the critical field. The positive value of $G_N - G_S$ shows that the superconducting state is more stable than the normal state. The quantity on the right hand side is the condensation energy of the superconducting state. Condensation energy is the energy gap between normal and superconducting electrons as predicted by the BCS theory (refer Figure 1.3) .Using $S = -\frac{dG}{dT}$, the difference in entropy density between the two states in zero field is

$$S_S - S_N = \frac{1}{2\mu_0}\frac{dB_c^2}{dT} = \frac{B_c}{\mu_0}\frac{dB_c}{dT} \quad (8)$$

and using $C = \frac{TdS}{dT}$, the difference in heat capacity per unit volume in zero field is

$$C_S - C_N = \frac{T}{2\mu_0}\frac{d^2B_c^2}{dT^2} = \frac{T}{\mu_0}[B_c\frac{d^2B_c}{dT^2} + (\frac{dB_c}{dT})^2] \quad (9)$$

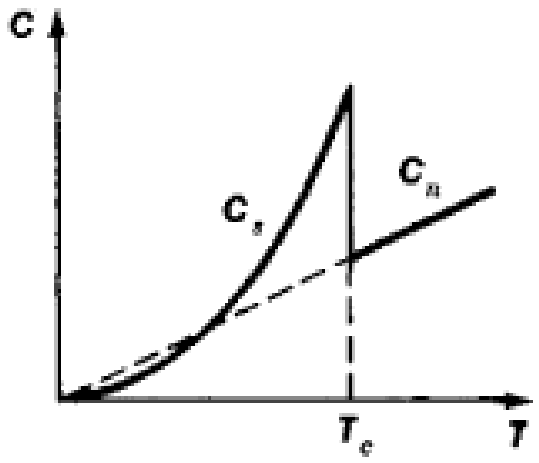

Figure 1.5 Heat capacity of normal and superconducting material | Source: McGraw-Hill Concise Encyclopedia of Physics |

Equations 8 and 9 enables us to make some important deductions about the specific heat curve of a metal in its normal and superconducting states. The entropy difference vanishes at the critical temperature T_c since B_c is zero (refer Figure 1.1). But specific heat difference is finite since $\frac{dB_c}{dT} > 0$. ΔS and ΔC vanish at T = 0 as expected from the third law of thermodynamics. For $0 < T < T_c$, $\frac{dB_c}{dT} < 0$. So $\Delta S < 0$. This explains why the superconducting state is more ordered than the normal state.

1.5 Magnetic Properties of Superconductors

Superconductors can be divided into three based on their behavior in a magnetic field. These are Type I, Type II and the more recent multigap (Type 1.5) superconductor. The physics of these systems is governed by two fundamental length scales namely the penetration depth λ and coherence length ξ.

1.5.1 Type I & Type II Superconductors

Type I superconductors lose their superconducting properties abruptly on applying the critical field B_c. They also show complete expulsion of magnetic flux from the interior of the sample. Type I superconductivity is shown by elements. Type II superconductors show Meissner effect

only up to a certain critical field B_{c1}. Above this field, there is partial flux penetration into the sample. But it still retains its superconducting properties. On increasing the field further to a field B_{c2}, the sample completely loses its superconducting property. The fields B_{c1} and B_{c2} are called lower and upper critical fields respectively. Type II superconductors are thus capable of withstanding higher fields when compared to Type I superconductors. Between B_{c1} and B_{c2}, the sample is said to be in the mixed state.

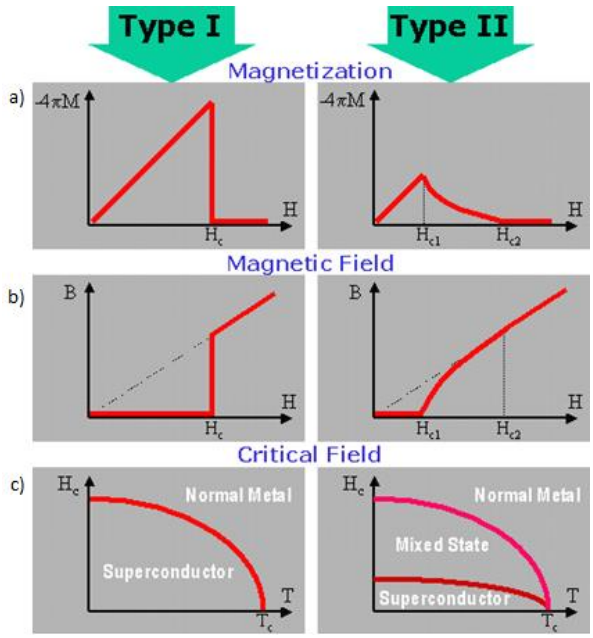

Figure 1.6 A comparison of Type I and Type II superconductors.

Figure 1.6 a) shows that magnetization in a Type I superconductor is equal and opposite to the applied field and drops to zero above the critical field. In a Type II superconductor, the magnetization is equal and opposite to the applied field up to the lower critical field, but decays slowly and finally becomes zero above the upper critical field. Figure 1.6 b) shows that the field inside a Type I superconductor is zero up to the critical field. Above this field, there is breakdown of superconductivity and the external applied field enters the sample. This is not the case in Type II superconductors, as was explained earlier.

The penetration of magnetic field into Type II superconductors occurs through vortices. The vortex has a normal core and is surrounded by a circulating supercurrent which cancels the

field in the superconducting region. The flux in each vortex is quantized in units of h/2e, where h is the Planck's constant and e is the charge of an electron. These vortices repel each other. Thus they form a hexagonal lattice called Abrikosov lattice. As the magnitude of external field is increased, the density of vortices increases. The vortex cores eventually overlap and the material becomes a normal conductor.

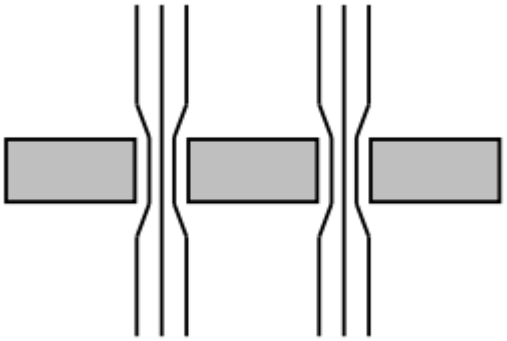

Figure 1.7 Magnetic flux entering the sample. | Source: Vortex Structure Formations in Type 1.5 Superconductors, Karl A H Sellin |

Vortices have a normal core with a size equal to the coherence length ξ and have supercurrents flowing around it over a distance equal to the penetration depth λ. In a type I superconductor, owing to its larger value of ξ compared to λ, the normal cores would overlap first. This leads to attraction between vortices. In a type II superconductor, its larger value of λ results in overlap of the supercurrents. This causes repulsion between vortices.

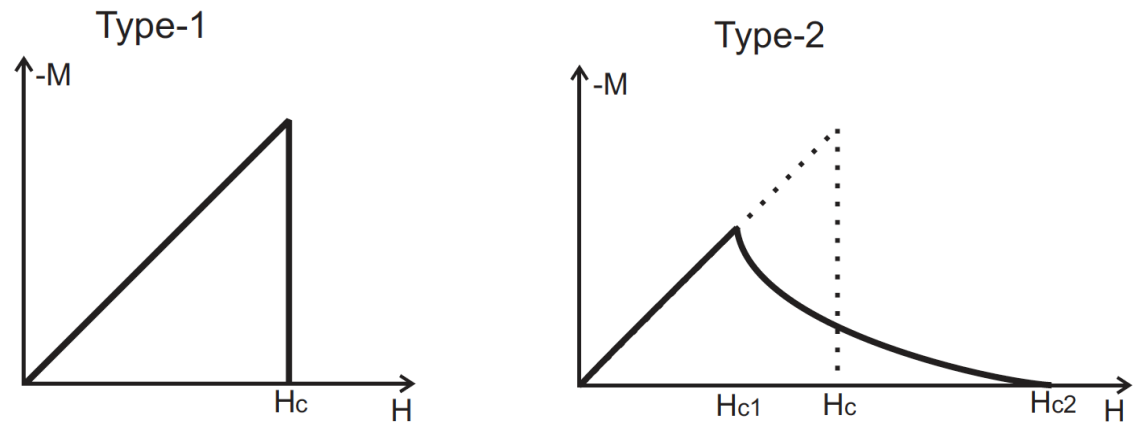

Figure 1.8 A comparison of the magnetization in a superconductor versus the applied magnetic field in type I and type II superconductor | Source: E. Babaev, J. Carlstrom, J. M. Speight Phys. Rev. Lett.105, 067003 (2010) |

Why do some materials show Type I superconductivity and others show Type II behavior?

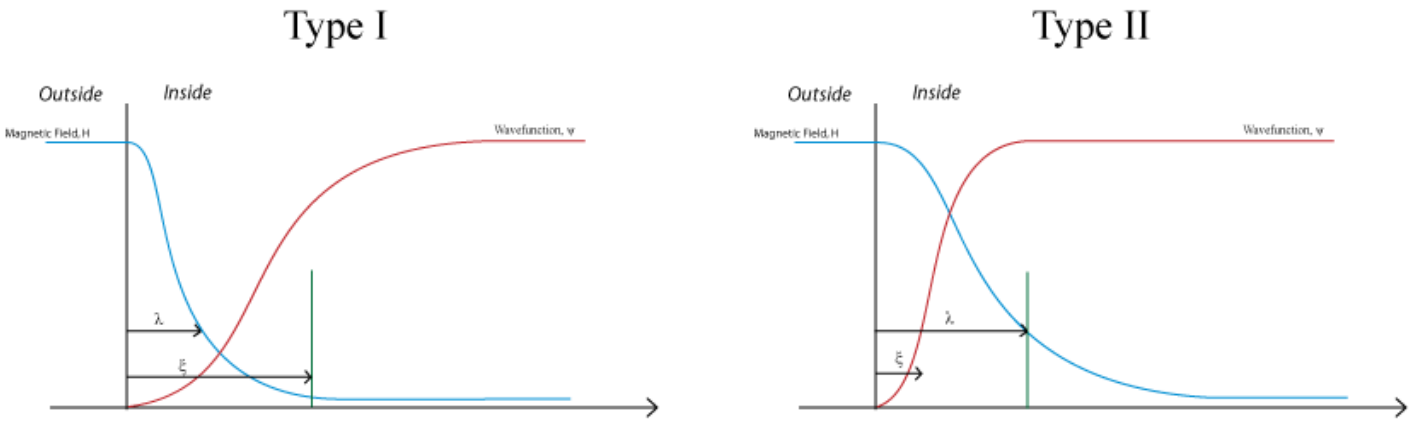

Figure 1.9 Relationship between coherence length and penetration depth in Type I and Type II superconductors | Source: http://www.doitpoms.ac.uk/tlplib/superconductivity/type.php |

A qualitative answer can be found by estimating the energy cost of forming a boundary between a normal and superconducting region. Since the normal and superconducting phases are at equilibrium at the critical field B_c, the free energies per unit volume on either sides of the boundary are equal. In the boundary region, there is a loss of condensation energy over a

distance of ξ at the boundary. This results in an increase in free energy

$$\Delta G_c \approx (G_N - G_S)\xi \quad (10)$$

The presence of the boundary allows the field to penetrate a distance λ causing a decrease in free energy given by

$$\Delta G_B \approx -\frac{B_c^2 \lambda}{2\mu_0} \quad (11)$$

Thus if the total energy associated with formation of boundary $\Delta G_B + \Delta G_C$ is positive, the material will try to avoid formation of boundaries. Such materials would show Type I behavior. Comparing equations (7), (10) and (11), we get the condition for Type I superconductivity to be $\xi > \lambda$. When $\xi < \lambda$, it becomes energetically favorable for the system to break up into a mixture of normal and superconducting regions. The decrease in energy due to the penetration of field into the superconducting regions compensate for the loss of condensation energy. Thus, for $\xi < \lambda$ Type II behavior is observed. For a type I superconductor, $\kappa < \frac{1}{\sqrt{2}}$ and for a type II superconductor ,$\kappa > \frac{1}{\sqrt{2}}$.

1.5.2 Multigap Superconductors (Type 1.5 Superconductors)

In multigap superconductors, superconducting components originate from electronic Cooper pairing in different bands. There are three fundamental length scales: two coherence lengths ξ_1 and ξ_2 and the magnetic field penetration length λ. So the model cannot be parameterized by a single dimensionless parameter κ. Multigap superconductors show vortex formation similar to that seen in Type II superconductors. The difference is that type 1.5 superconductors have non-monotonic vortex interaction. The vortices are attractive over long range due to dominant density-density interaction and repulsive over short range due to current-current and electromagnetic interactions. This non-monotonic interaction results in the formation of vortex clusters in low magnetic field, surrounded by vortexless areas (Figure 1.8 a,b). This state is often called semi Meissner state.

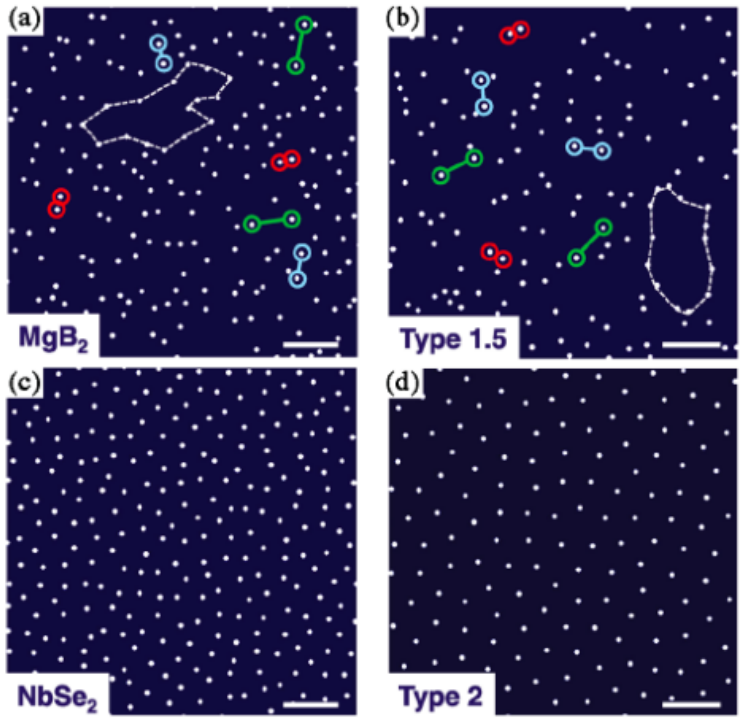

Figure 1.10 Vortex cluster formation in Type 1.5 superconductors versus vortex lattice formation in Type II superconductor | Source: V.V. Moschalkov et al PRL 2009 |

Since the vortices form clusters, magnetic response of the system cannot be explained merely by considering the energy of normal to superconductor state boundary (as described in the end of section 1.5.1). In such a system, the energy per vortex depends on whether the vortex is placed in a cluster or elsewhere. Thus, both energy of a vortex in a cluster and the energy associated with the boundary of a cluster determine vortex formation. The system tends to minimize the boundary energy of a cluster as seen in type I systems. However, within the cluster, the vortices form a lattice similar to type II systems.

Thus to summarize, type 1.5 superconductivity is seen typically in systems for which $\xi_1 < \sqrt{2}\lambda < \xi_2$. The intervortex interaction is attractive at long range but repulsive at short range. Within a cluster, the normal to superconductor state boundary energy is negative, which is why vortex formation is favoured. But the vortex cluster to normal state boundary energy is positive. At low external magnetic fields, type 1.5 superconductors show Meissner effect. At intermediate fields, it exists in a semi – Meissner state. Vortex clusters coexist with Meissner

domains. At larger fields, vortices are arranged into lattices. Eventually, on increasing the field even further, the system loses its superconductivity. Figure 1.9 shows that the vortices in a type 1.5 superconductor are formed via first order phase transition. The transition from vortex state to normal state is second order.

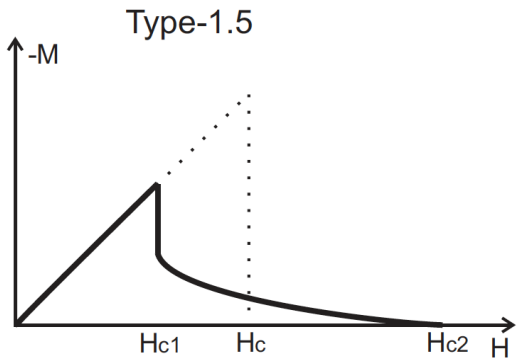

Figure 1.11 Magnetization in sample versus applied magnetic field graph for type 1.5 superconductor | Source: E. Babaev, J. Carlstrom, J. M. Speight Phys. Rev. Lett.105, 067003 (2010) |

Chapter 2

Experimental Techniques

2.1 Synthesis of OsB_2 and RuB_2

Polycrystalline samples of OsB_2 and RuB_2 were prepared by the process of arc melting in tetra arc furnace. OsB_2 has been reported to melt congruently at around 1870˚C. OsB_2 samples were prepared using Os powder (99.95%, Alfa Aesar) and B chunks (99.999%, Alfa Aesar).The constituent elements were taken in stoichiometric proportions. They were melted on a water cooled copper puck in high purity argon atmosphere. A titanium getter was used to remove any trace of oxygen in the chamber. Os powder, being extremely light, has a tendency to fly off due to the arc pressure of the electrodes. To overcome this problem, Os was first pelletized before melting. The sample was flipped over and melted 6-10 times to ensure homogenous melting. The sample was weighed after the initial melts and any weight loss due to evaporation of boron was compensated by adding the required amounts of boron in the subsequent melts. RuB_2 was similarly synthesized using Ru powder (99.99%, Alfa Aesar) and B chunks (99.999%, Alfa Aesar). These samples were subsequently crushed or cut for future measurements.

2.1.1 Tetra Arc Furnace

Tetra arc furnace is used to grow crystals of compounds that melt congruently. The sample is placed on a copper puck in between four electrodes that use an electric arc to heat the sample

uniformly from all four directions. The melting is carried out in a high purity argon environment. The argon gas provides an inert atmosphere that prevents the contamination of the sample. It also provides a medium for electric arc discharge that would have been otherwise impossible in vacuum. The copper puck is continuously cooled with water at 17˚C to prevent copper from melting and contaminating the sample. Prior to heating the sample, a titanium getter is heated. At high temperatures, titanium can absorb oxygen and this purifies the chamber further. Arc melting is usually used for compounds that have relatively high conductance. The sample gets heated due to its resistivity. So higher resistivity would imply that the sample would reach higher temperatures. But if the resistivity is too high, the arc would not come in contact with the sample. It would ignore the sample and would come in contact with the puck which is at ground potential.

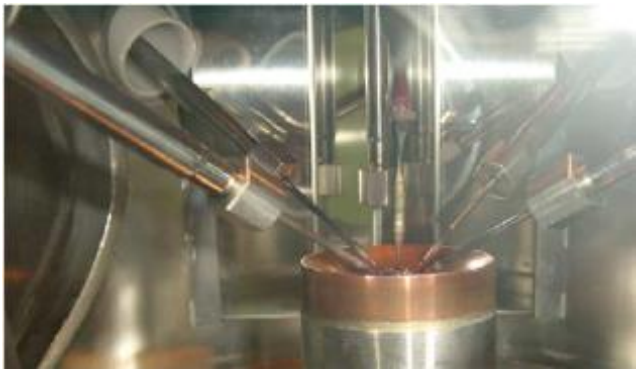

Figure 2.1 The interior of tetra arc furnace with four electrodes and a copper puck to place sample. | Source: M. Szlawska and D. Kaczorowski |

2.1.2 Single Crystal Growth

The compound prepared by arc melting is polycrystalline in nature. To understand multigap superconductors better, it is necessary to study how its superconducting properties vary with direction. Studies on MgB_2 show that its critical field was considerably higher when magnetic field was applied along c-axis when compared to critical field when magnetic field applied perpendicular to c-axis. Similar studies have to be carried out in OsB_2 and RuB_2 as well. In order to study the directional properties of the compound we need single crystals that are

oriented in a particular direction. Single crystal growth of OsB_2 and RuB_2 were attempted by two methods, namely, Czochralski method and Cu-B eutectic flux growth method.

In the Czochralski method, the sample is melted in the tetra arc furnace. The arc furnace comprises of a fifth electrode vertically above the puck as shown in Figure 2.1. This electrode is capable of rotation and can also move up and down. The tip of the electrode is brought in contact with the molten sample and is pulled upwards in a controlled rate to ensure that the pull rate is less than the rate of crystallization. This required rate is determined by trial and error.

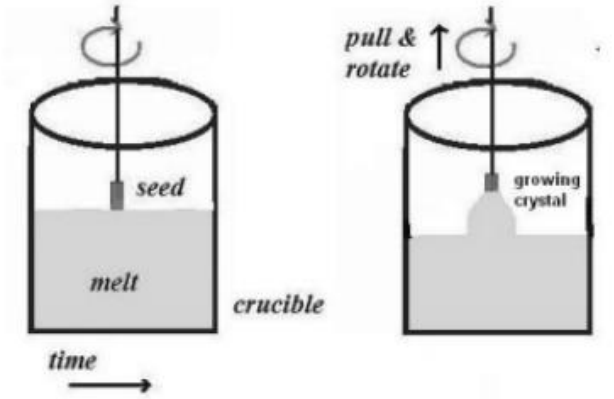

Figure 2.2 Schematics of Czochralski growth. | Source: shodhganga.inflibnet.ac.in |

In flux growth method, first a polycrystalline sample of OsB_2 is prepared. A Cu-B binary alloy is prepared at the eutectic composition $Cu_{0.87}B_{0.13}$ by arc melting. The arc melted OsB_2 sample is melted with the Cu-B alloy. For crystal growth, the sample is placed in an Al_2O_3 crucible and covered with a lid. It is placed in a furnace which is evacuated and purged with high purity argon gas repeatedly. The growth was started in a flow of argon. The furnace is heated to 800˚C in 30 minutes, then heated to 1450˚C in 6 hours and held at this temperature for 6 hours. The furnace is cooled to 1020˚C at the rate of 2˚C/hour and then rapidly cooled to room temperature. The Cu-B flux is dissolved in dilute nitric acid.

2.2 Characterization of Sample

Once the sample has been prepared, we need to ensure that the sample prepared is indeed our required compound (in this case OsB_2 or RuB_2). So, in order to determine this, the X-Ray Diffraction (XRD) measurements were carried out on the powdered sample.

2.2.1 X-Ray Diffraction

X-ray diffraction is a very important experimental technique that can give information about the crystal structure of bulk solids, including lattice constants and geometry, orientation of single crystals, and preferred orientation of polycrystals, defects, stresses, etc. Diffraction of light by crystals is similar to that of an optical grating consisting of several parallel lines drawn on a glass plate. As light is incident on the grating, each group will act as a line source and light will be radiated in all directions. Interference occurs between the waves and in a certain direction, constructive interference occurs. In all the other directions destructive interference occurs reducing the intensity. In the case of a grating, the condition of constructive interference can be written as $n\lambda = d \sin\theta$, where d is the distance between the grooves and is θ the angle of observation. For the first order diffraction, $\lambda = d \sin\theta$. In Bragg's law, a crystal is considered as a plane containing several lattice points. The reflection of X-rays will take place from these planes with the angle of reflection being equal to the angle of incidence. The reflected beams are in phase when the path length between the beams is an integral multiple of the wavelength. The planes of light travelling after reflection will be in phase only when this condition is satisfied. For all other angles, destructive interference leads to cancellation of the intensity. For crystals containing thousands of such planes, Bragg's law imposes severe restrictions on the angle required for destructive interference and the cancellation of intensities is usually complete.

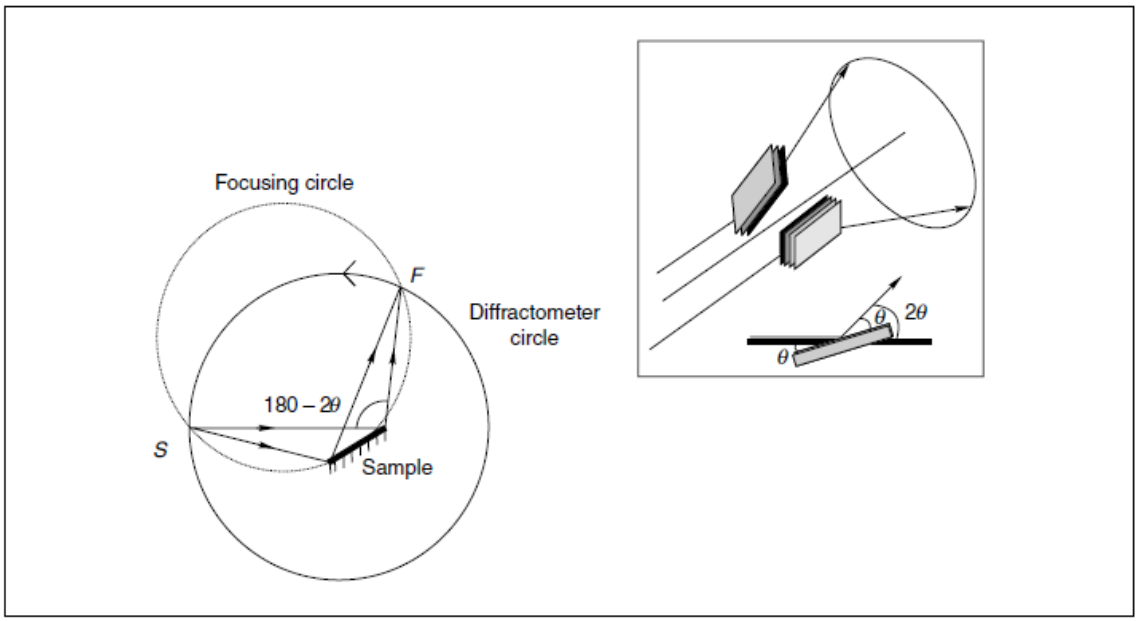

Figure 2.3 XRD setup where S is the X-ray source and F is the detector.

X-ray diffractometer typically consists of three basic elements: an X-ray tube, a sample holder, and an X-ray detector. A filament is heated in a cathode ray tube to produce electrons. The electrons are accelerated towards a target by applying a voltage. X ray is produced when electrons have sufficient energy to dislodge inner shell electrons of the target material. Copper is usually used as the target material with Cu K_α wavelength of 1.5418Å. These X-rays are collimated and directed onto the sample. The intensity of the reflected X-rays is recorded as the detector and sample are rotated. When constructive interference occurs, a peak in intensity occurs. A detector records and processes this X-ray signal and converts the signal to a count rate which is then output to a device such as a printer or computer monitor. The sample rotates in the path of the collimated X-ray beam at an angle θ while the detector that collects the diffracted X-rays rotates at an angle of 2θ.

2.2.2 Understanding powder diffraction patterns

A typical XRD pattern is shown in Figure 2.4. In order to discern the chemical composition and orientation of the sample, there is a need to understand how structural information is

encoded in a XRD pattern. This information is embedded mainly in three components: positions, intensities and shapes of the Bragg diffraction peaks.

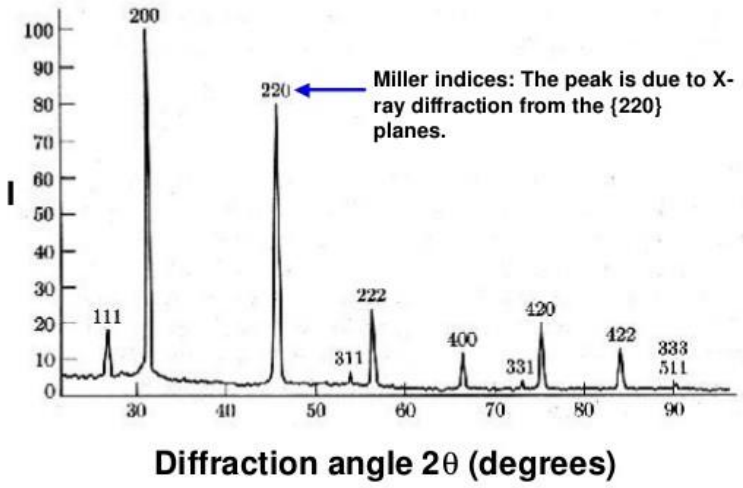

Figure 2.4 XRD pattern of NaCl powder | Source: http://www.slideshare.net/chem_engine/x-ray-diffraction-39221132 |

The peak position gives unit cell parameters (a, b, c, α, β, γ), symmetry and content. The peak intensity gives atomic parameters (x, y, z etc.), coordinates of atoms and space group symmetry. The peak shape gives information about crystallinity, defects and dislocations in the sample. From Bragg's law,

$$2d_{hkl}sin\theta = \lambda \qquad (12)$$

λ is known to be 1.54 Å for Rigaku diffractometer which uses Cu-Kα radiation. The value of sinθ for various peaks can be found by substituting the value of θ from the x-axis of the XRD pattern. Substituting all these parameters in the above equation gives the value of d_{hkl}, the inter-planar spacing. Now this value of d_{hkl} can be used to find parameters a, b, c using the equation

$$d_{hkl} = (\frac{h^2}{a^2} + \frac{k^2}{b^2} + \frac{l^2}{c^2}) \qquad (13)$$

The peak intensity is given by the area under the peak and it is the relative intensities between the various peaks that gives information about arrangement of various atoms in the unit cell. The absolute values of intensities have very little meaning in structure determination. The

scattering from electrons, scattering from an atom and scattering from a unit cell contribute to the peak intensity. An atom with more number of electrons will scatter more of the incoming x-ray. Even if Bragg's law is satisfied by a particular set of (h, k, l) values, the peak may be absent in the XRD pattern due to presence of additional atoms in the unit cell. Thus the presence or absence of a particular set of peaks can provide information about the Bravais lattice of the sample.

Bravais Lattice	**Allowed Reflections**
Simple Cubic	All
Body Centered Cubic	(h+k+l) even
Face Centered Cubic	h, k and l are all odd or all even

Table 2.1 This table shows how certain sets of (h, k, l) values can be used to determine structure.

2.2.3 Refinement of XRD data

The theoretical XRD line profile is often different from the measured data. This is because the shape of the measured powder diffraction pattern is influenced by temperature, characteristics of the beam, experimental arrangement sample size etc. Thus, in order to get precise information about the sample, there is a need to refine the theoretical line profile until it best matches the measured profile. A software called GSAS was used for XRD refinement. An unidentified powder diffraction pattern is first compared with known powder patterns. This helps to identify the specific elements, density, unit cell structure etc. If the pattern cannot be identified in a database, we try to find the unit cell and assign indices to the reflection patterns. This structure is then refined using the Rietveld method wherein all parameters, unit cell profile and structure parameters are refined in one process.

Effect in diffraction pattern	**Possible Causes**
Wrong absolute intensities	Weight fraction/scaling
Wrong relative intensities	Preferred orientation effect Atomic coordinates Site occupancies Thermal displacement parameters
Wrong peak width	Crystallite size Lattice strain

Table 2.2 This table shows the possible reasons for difference in XRD pattern of theoretical model and experimental XRD data.

In order to observe diffraction, a crystal has to be placed in the X-ray beam in such a way that it fulfills the Bragg condition for diffraction. In the case of single crystal diffractometers, the crystal can be rotated in the beam about different axes in order to position a lattice plane for diffraction. However, in powder diffraction, ideally there is an infinite number of crystals in the beam. Thus in practice, there are several crystals always available for diffraction for each lattice plane. Each plane scatters at a distinct 2θ angle and thus gives a set of concentric rings, each representing a specific lattice plane. However, if crystallites in a powder sample have, say, needle or plate like shape, they may not necessarily adopt random orientations. They have a tendency to be oriented in a particular direction due to structural constraints. This is called preferred orientation effect and it causes a systematic error in peak intensities.

Theoretical models assume the atoms to be stationary but the atoms vibrate around their equilibrium positions at even 0 K. Thus, the atom is interpreted to be stationary by the X-rays, but is displaced in some random manner from its average location. This apparent spread of an atom over a region due to its vibrational motion causes the scattering amplitude to decrease much faster at high values of θ than that of a stationary atom. To take into consideration the effect of atomic vibrations, atomic scattering factor at temperature T is introduced and is written as

$$f_T = f_0 exp(-Bsin^2\theta/\lambda^2) \quad (14)$$

$$B = 8\pi^2 U \quad (15)$$

where B is called the temperature factor and U is the mean square displacement of each atom from its average position and is usually in the range 0.1 – 0.3 angstrom. The simplest assumption that atomic displacement is isotropic requires only a single term B_{iso} to describe its motion. However, crystals seldom have isotropic environment. Thus, atomic motion is often described in terms of an ellipsoid with larger amplitudes of vibration along a particular direction than others. This gives six parameters for each atom.

The effects described above in addition to many other factors are all taken into consideration in order to refine a theoretical model so that it matches experimental conditions. Once the model has been refined, there is a need to know quality of refinement. There are several values that can be used to distinguish a good refinement from a poor one such as goodness-of-fit, R factors etc. Diffraction data is generally a set of intensity values collected as a function of 2θ values [1]. The intensity values are labelled $\mathbf{y_{o,i}}$ and indicates that these values are observed values of intensity measured at $2\theta_i$. Reitveld analysis requires an uncertainty estimate for $\mathbf{y_{o,i}}$ labelled $\boldsymbol{\sigma}\mathbf{[y_{o,i}]}$. This uncertainty means that if there is a true value of intensity ($\mathbf{y_{t,i}}$) , which can be obtained by measuring it an infinite number of times, then on an average $\mathbf{y_{o,i}}$ will be deviate from $\mathbf{y_{t,i}}$ by ± $\boldsymbol{\sigma}\mathbf{[y_{o,i}]}$. In Rietveld analysis, a theoretical model is fitted to the experimental data. The intensity value simulated from the model is labelled $\mathbf{y_{c,i}}$. The Rietveld algorithm minimizes $\sum_i w_i(\boldsymbol{y}_{\mathbf{c,i}} - \boldsymbol{y}_{o,i})^2$ where $w_i = 1/\boldsymbol{\sigma}^2[\boldsymbol{y}_{\mathbf{o,i}}]$. The weighted profile R factor $\mathbf{R_{wp}}$ is an indicator of this discrepancy factor and is given as $R_{wp}^2 = \sum_i w_i(\boldsymbol{y}_{\mathbf{c,i}} - \boldsymbol{y}_{o,i})^2 / \sum_i w_i(\boldsymbol{y}_{o,i})^2$. The ideal model would accurately predict the true value for each $\mathbf{y_{o,i}}$. Similarly each model has a maximum limit to the best possible value that can ever be obtained for a set of data that is usually constrained by the number of data points, number of refinement parameters etc. This best possible value of $\mathbf{R_{wp}}$ is called the expected R factor $\mathbf{R_{exp}}$. Another indicator of the quality of fit is χ^2 often called the goodness-of-fit and is determined from the R factors as $\chi^2 = \frac{\left(\frac{1}{N}\right)\sum_i(\boldsymbol{y}_{\mathbf{c,i}} - \boldsymbol{y}_{o,i})^2}{\boldsymbol{\sigma}^2[\boldsymbol{y}_{\mathbf{o,i}}]} = \left(\frac{R_{wp}}{R_{exp}}\right)^2$. Initially, χ^2 is large when the model is poor and decreases as the model is refined. χ^2 should never drop below 1 and if a refinement results in $\chi^2 < 1$, it indicates two possibilities. Either the standard uncertainties have been overestimated or so many parameters have been introduced that the model tries to fit noise as well. Values of $\chi^2 \approx 1$ does

not necessarily imply that the model is correct. There could be models that produce good fit but lack of sufficient experimental data prevents fitting of a complex or better model. If refinement results in $\chi^2 >> 1$, then various possibilities are that the model is reasonable but the standard uncertainty values are underestimated or that the model is incomplete because there are systematic errors in the data that are not expressed in the model or that the model is wrong. Despite the existence of all the above mentioned parameters to determine the quality of refinement, there is no rule of thumb to determine a threshold value that indicates that a refinement is reliable. These indices are a measure of not just how well the structural model fits the diffraction intensities, but also of how well the background, diffraction positions and peak shapes have been fit. If the background contributes to a large percentage of the total intensity in a pattern, then fitting the background alone can give relatively small χ^2 or R_{wp} values, even without a valid structural model.[2] High χ^2 values can occur where data are collected to very high precision. Minor imperfections in the fit become huge with respect to the experimental uncertainty. In such cases, χ^2 can be deceptive and should be interpreted with discretion.

2.2.4 Physical Property Measurement System

Once the required crystal has been obtained, we need to verify that it is indeed a superconductor and study its other properties as well. These measurements are carried out in a Physical Property Measurement System (PPMS, Quantum Design). The PPMS is a fully automated variable temperature and magnetic field system that can measure thermal transport, heat capacity, electro transport etc. Temperatures can be varied from 0.4 K to 400 K and has a magnetic field that can reach up to 9 Tesla. With a ^{3}He system, the temperature can go down to 350 mK. Measurements are usually made by passing a known current through the sample and measuring the voltage drop across it.

Figure 2.5 (left) 12 pin connection; (middle) heat capacity microcalorimeter puck; (right) AC transport puck | Source: Properties of Materials: Physical Property Measurement System (PPMS) Institute for Research in Materials (IRM) Dalhousie University |

Figure 2.6 One of the sample platforms available to hold the sample puck.| Source: Properties of Materials: Physical Property Measurement System (PPMS) Institute for Research in Materials (IRM) Dalhousie University |

Several sample pucks are available that can be installed into the chamber according to the measurement that is to be carried out. To carry out resistivity measurements, the sample is

mounted on an AC transport puck. Leads are attached to the sample with solder or silver epoxy paste. The paste is allowed to dry for a day before it is loaded on the platform.

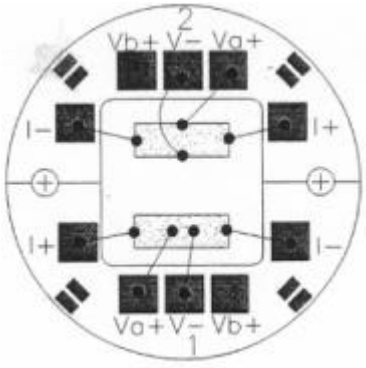

Figure 2.7 Arrangement of sample on AC transport puck for resistivity measurement using four probe method. | Source: Properties of Materials: Physical Property Measurement System (PPMS) Institute for Research in Materials (IRM) Dalhousie University |

The measurement is carried out using four probe method which offers several advantages over the usual two probe method. At low temperatures, the resistivity of the sample falls drastically in superconductors. In order to measure these small values precisely, it is necessary that the resistance of the leads and contacts (which are comparably very large) do not affect the measurements. This is achieved by the four probe method.

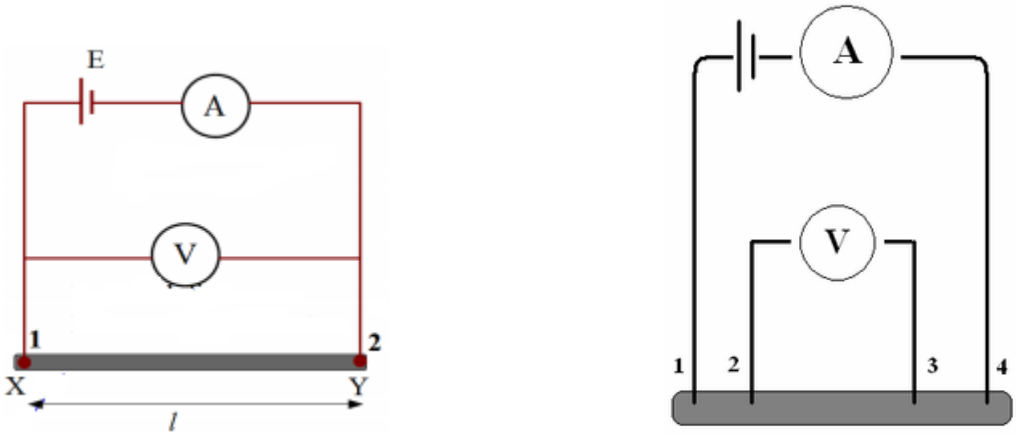

Figure 2.8 A schematic diagram showing two probe versus four probe measurement. | Source: Wikipedia |

In the four wire resistance measurement, current is passed through the sample via two current leads and the potential difference across the sample is measured via two separate voltage leads. The leads connected to the voltmeter draw very little current due to high impedance of the voltmeter. The voltage drop at points 2 and 3 in Figure 2.8 due to contact resistance between probe and sample is also eliminated. The measurements can be carried out in two modes i.e. the AC and DC mode. In AC mode, DC excitation is applied to the sample and potential drop is found. Then the current is reversed and potential drop is noted again. The readings are averaged to provide value of potential difference. This method eliminates any voltage difference produced in the sample due to effects like change in temperature. Suppose the potential difference when current is applied in the forward direction is given as

$$V_{forward} = V_{current} + V_{other} \quad (16)$$

where $V_{current}$ is the potential drop due to the current, V_{other} is the potential drop due to effect of instrumentation, temperature etc. Now, the reversal of current causes reversal in direction of potential drop.

$$V_{backward} = -V_{current} + V_{other} \quad (17)$$

Subtracting the two equations give

$$V_{current} = \frac{V_{forward} - V_{backward}}{2} \quad (18)$$

In DC mode, two consecutive voltage readings that have identical polarity are averaged. This mode gives less accurate voltage readings than AC mode, but is useful in situations where reversing polarity would affect the sample.

In order to study superconductivity, resistivity has to be measured at low temperatures as well. This is achieved using liquid ^{4}He and ^{3}He. Helium in the gas phase undergoes condensation by Joule Thomson expansion which takes place after the ^{4}He-^{3}He mixture is precooled in a Joule Thomson heat exchanger. Joule Thomson effect is the change in temperature of a gas during adiabatic expansion. Joule Thomson (JT) coefficient ($(\frac{dp}{dT})_H$) determines if the gas gets heated up or undergoes cooling during expansion. A positive coefficient indicates that the gas

undergoes cooling upon expansion. Helium has a positive JT coefficient only below 43K. This is why the helium mixture is precooled in a heat exchanger. Once cooled to the requisite 43K, Joule Thomson effect is employed for further cooling. Gas under high pressure is allowed to expand through a capillary section, thus cooling it. This cooled gas is used to pre-cool the next cycle of incoming gas. This new cycle of incoming gas, being cooler than the first cycle, cools to even lower temperatures by expansion. The cycle is repeated until the helium mixture is liquefied. The minimum temperature that can be achieved by this method is about 4.2 K. Lower temperatures can be achieved by pumping over liquid helium. This cause the molecules of the liquid to evaporate and causes cooling of the remaining liquid. The expression given below shows that vapor pressure decreases exponentially with temperature [24].

$$p = constant.e^{(\frac{-L}{RT})} \quad (19)$$

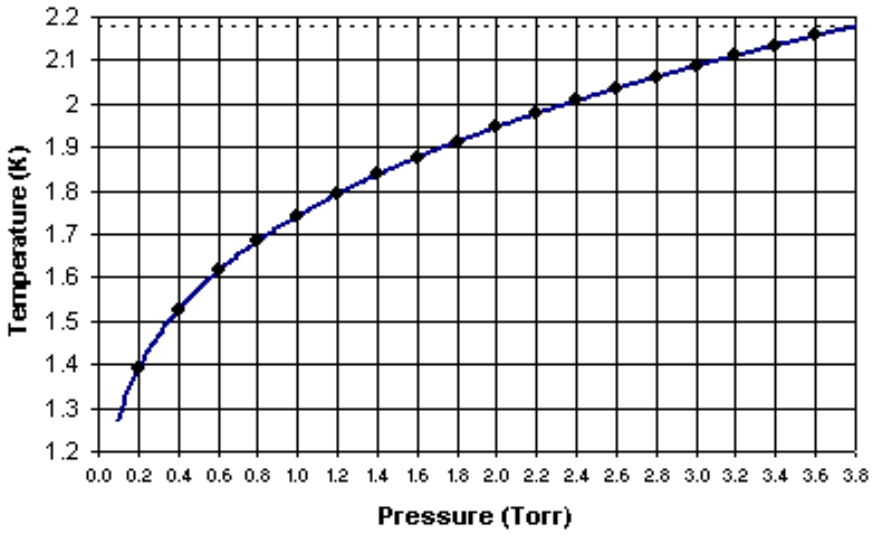

Figure 2.9 Temperature versus vapour pressure of liquid helium | Source: http://mxp.physics.umn.edu/s04/projects/s04he/theory.htm |

The minimum temperature accessible using ^{4}He is limited to 1.3 K but this can be extended to 0.3 K if ^{3}He is used. The main reason that we are able to attain lower temperatures with ^{3}He is due to the difference in vapour pressure of the two isotopes at the same temperature. The ratio of vapour pressure of ^{3}He to ^{4}He is 74 at 1 K and around 10^4 at 0.5 K.

Vibrating Sample Magnetometer systems are used to measure the magnetic properties of materials as a function of magnetic field, temperature, and time. The basic principle of operation for a vibrating sample magnetometer is that a changing magnetic flux will induce a voltage in a pickup coil. The time-dependent induced voltage is given by the following equation

$$V_{coil} = \frac{d\phi}{dt} = (\frac{d\phi}{dz})(\frac{dz}{dt}) \quad (20)$$

where Φ is the magnetic flux enclosed by the pickup coil, *z* is the vertical position of the sample with respect to the coil, and *t* is time. For a sinusoidally oscillating sample position, the voltage is given by

$$V_{coil} = 2\pi fCmAsin(2\pi ft) \quad (21)$$

where *C* is a coupling constant, *m* is the DC magnetic moment of the sample, *A* is the amplitude of oscillation, and *f* is the frequency of oscillation. The magnetic moment is acquired by measuring the coefficient of the sinusoidal voltage response from the detection coil. In a VSM, a sample is placed within sensing coils, and is mechanically vibrated. The resulting magnetic flux changes induce a voltage in the sensing coils that is proportional to the magnetic moment of the sample. The sample to be studied is first placed in a constant magnetic field. If the sample is magnetic, this constant magnetic field will magnetize the sample by aligning the individual magnetic spins with the field. The stronger the constant field, the larger the magnetization will be. The magnetic dipole moment of the sample will create a magnetic field around the sample, called the magnetic stray field. As the sample is moved up and down, this magnetic stray field changes as a function of time and can be sensed by a set of pick-up coils. The alternating magnetic field will cause an electric field in the pick-up coils. This current is proportional to the magnetization of the sample. The induction current is amplified and the system tells how much of the sample is magnetized and how its magnetization depends on the strength of the constant magnetic field [3].

Pressure studies are also carried out on the samples in the PPMS with the help of high pressure cell. The cell is a Beryllium Copper (BeCu) cylindrical cell for pressuring samples. The

maximum pressure that can be applied is 1.3 GPa. A teflon sample tube and teflon caps are used to form the high pressure seal. One end of the of the teflon sample tube is sealed with a teflon cap. The teflon sample tube is placed into the center cylinder leading with the open end of the teflon sample tube.

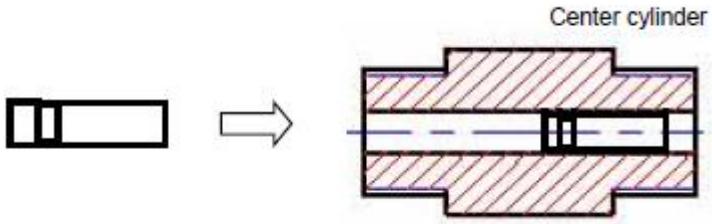

Figure 2.10 The teflon tube which has been closed only at one end is first inserted into the center cylinder. | Source: High Pressure Cell User Manual For use with the QD MPMS, PPMS VSM, and VersaLab VSM systems |

The sample and pressure transmitting media are inserted into the open end of the teflon sample tube. About 1mm length of Sn or Pb wire is also inserted leaving enough space at the top of the teflon sample tube to allow the second teflon cap to be inserted. The pressure cell kit includes Daphne 7373 oil as a pressure transmitting media which is applied into the sample tube with the help of a syringe. The second end of the sample tube is sealed with a teflon cap. Using the appropriate diameter sample push rod, the teflon sample tube is carefully pushed so that it is roughly centered within the center cylinder. The two pistons are inserted into the center cylinder.

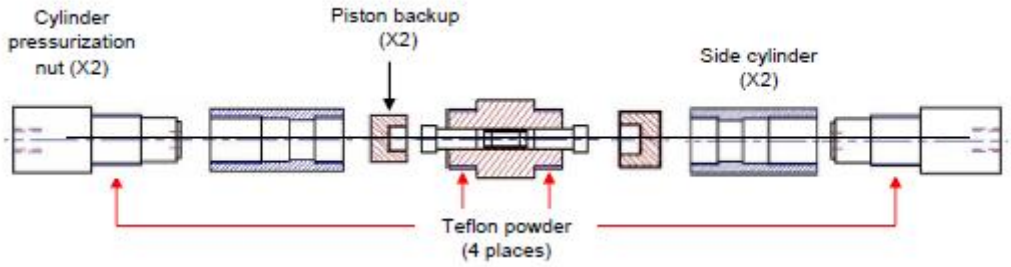

Figure 2.11 A view of the final cell assembly. | Source: High Pressure Cell User Manual For use with the QD MPMS, PPMS VSM, and VersaLab VSM systems|

The pressurization nut is initially finger tightened and to attain higher pressures, it is tightened with pressurization spanners. The pressure cell length is measured each time after pressure is applied and is used as reference so that the amount of compression can be determined later [4].

Chapter 3

Results and Discussions

3.1 Multigap Superconductors

In the quest to achieve superconductivity at room temperatures, the discovery of superconductivity in MgB_2 [10] at unusually high critical temperature (T_c = 39 K) has sparked interest in other metal diborides. Apart from this high temperature, the existence of more than one superconducting energy gap in MgB_2 was another interesting characteristic. One theory suggests that these peculiar characteristics arise from two separate groups of electrons that form different kinds of bonds. Structurally MgB_2 consists of hexagonal honey-combed planes of B atoms separated by planes of Mg atoms, with the Mg atoms centered above and below the B hexagons.

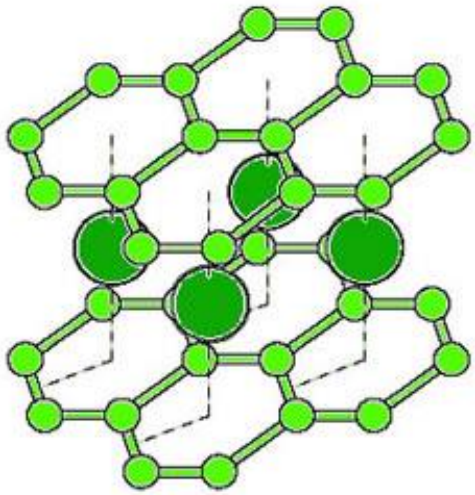

Figure 3.1 Structure of MgB_2 in which hexagonal honeycomb layers of B atoms alternate with layers of Mg atoms. | Source: http://www2.lbl.gov/Science-Articles/Archive/MSD-superconductor-Cohen-Louie.html |

MgB_2 has strong sigma bonds in the plane and weak pi bonds between them. Since boron atoms have fewer number of electrons than carbon atoms, all sigma bonds in boron plane are not occupied. Due to this, the lattice vibration in the boron planes has a much stronger effect, resulting in the formation of strong electron pairs confined to the planes. Apart from the strongly bonded sigma pairs, the boron electrons involved in pi bonds form much weaker pairs. This implies that electrons on different parts of the Fermi surface form pairs with different binding energies. Figure 3.2 shows the Fermi surface structure of MgB_2 made of four different kinds of sheets. The two nested cylinders colored red and orange represent the differently oriented sigma bond. They correspond to a large superconducting gap of $\Delta_\sigma(0) = 7.1meV$ [5][6][7]. Two other sheets of Fermi surface form tunnels and are depicted in blue. They represent pi bonded electrons and have a smaller superconducting gap of $\Delta_\pi(0) = 2.2meV$ [8][9].

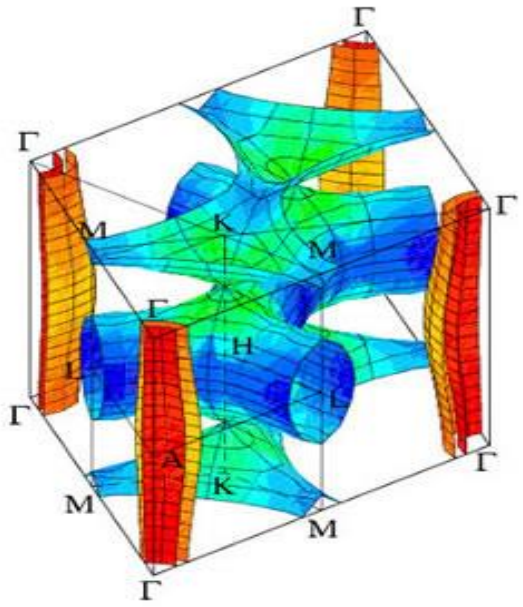

Figure 3.2 The size of superconducting energy gaps varies anisotropically depending different sections of MgB_2's complex Fermi surface. | Source: http://www2.lbl.gov/Science-Articles/Archive/MSD-superconductor-Cohen-Louie.html |

The superconducting energy gap in MgB_2 is reported to have s- wave symmetry which means that the gap is of the same sign and is non-zero everywhere on the Fermi surface. The size of the gap varies on different sections of the Fermi surface. The magnitude of the energy gap at 4K varies from 6.4 to 7.2meV on the σ sheets and from 1.2 to 3.7meV on the π sheets. The large energy gap of the σ-bonding states changes more slowly at low temperature and more rapidly near the critical temperature. Even though distinct superconducting gaps exist on different disconnected sheets, interband pairing leads to a single critical temperature [12][13]. Thus, both the σ and π gaps vanish at the same critical temperature.

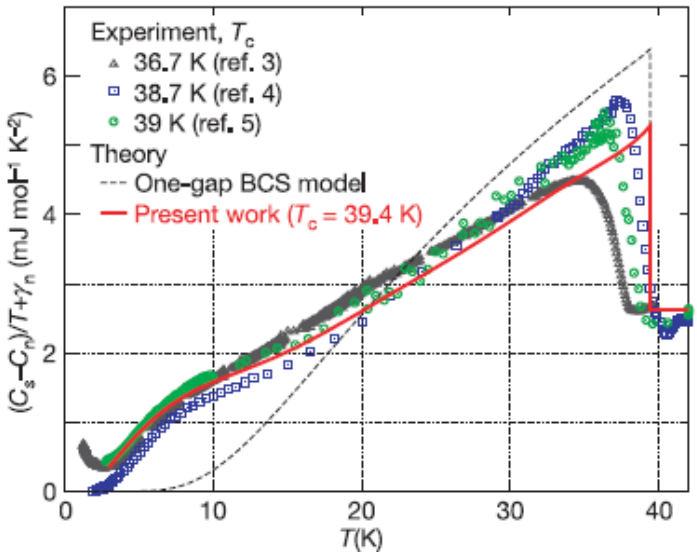

Figure 3.3 Specific heat versus temperature of MgB_2 | Source: H. J. Choi et al., Nature (London) 418, 758 (2002) |

Studying the specific heat versus temperature graph of MgB_2 gives a direct quantitative comparison of how multigap superconductors deviate from BCS model. MgB_2 has a substantial value of specific heat at low temperatures as shown in Figure 3.3. A kink also appears around 10K that doesn't appear in a one gap BCS model. This kink is reported to be caused by the existence of low energy excitations that take place across the small superconducting energy gap of π bonding states [11]. Among binary diborides with structures similar to MgB_2, superconductivity has also been reported in ZrB_2 ($T_c \approx 5.5K$) [14], NbB_2 ($T_c \approx 0.6K$) [15] and TaB_2 ($T_c \approx 10K$) [16].

3.2 Crystal Structure

Here, superconducting properties of OsB_2, RuB_2 and $LuRuB_2$ have been studied. The compounds were prepared by arc melting which has been described in detail in Chapter 2. In order to verify that the compounds had formed, XRD measurements were carried out on the sample.

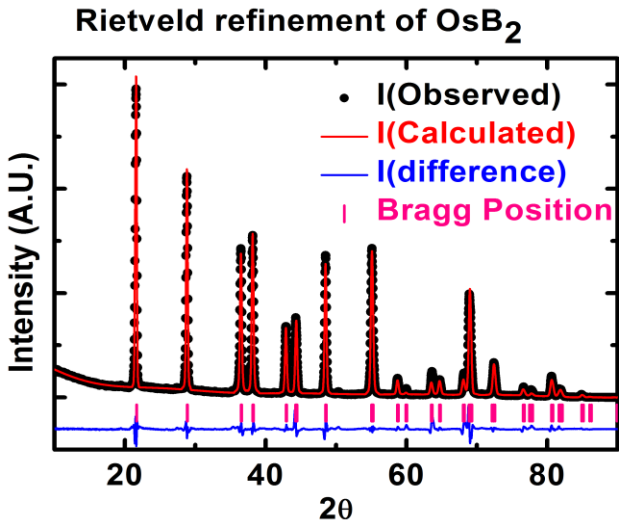

Figure 3.4 Refined XRD pattern of OsB_2 in which the black line represents experimental data, the red line is the fitted pattern and the blue line represents the difference between the observed and calculated intensities.

Space group name P m m n (No. 59)
Lattice parameters
a=4.694Å, b=2.875Å, c=4.080Å,
α=90° , β=90° , γ=90°
Unit-cell volume = 55.077975 Å^3
Structure parameters

Atom	x	y	z
Os	0.25	0.25	0.152
B	0.049	0.25	0.359

Figure 3.5 Lattice and structure parameters of OsB_2 extracted from XRD pattern.

All the lines in the XRD pattern of both OsB_2 and RuB_2 were identified to match orthorhombic *Pmmn* structure. P denotes that it is a primitive cell. The two 'm' denote mirror symmetry about x and y axis and n denotes glide symmetry about z axis. The lattice parameters show that $a \neq b \neq c$ and $\alpha = \beta = \gamma$ and thus confirm orthorhombic structure.

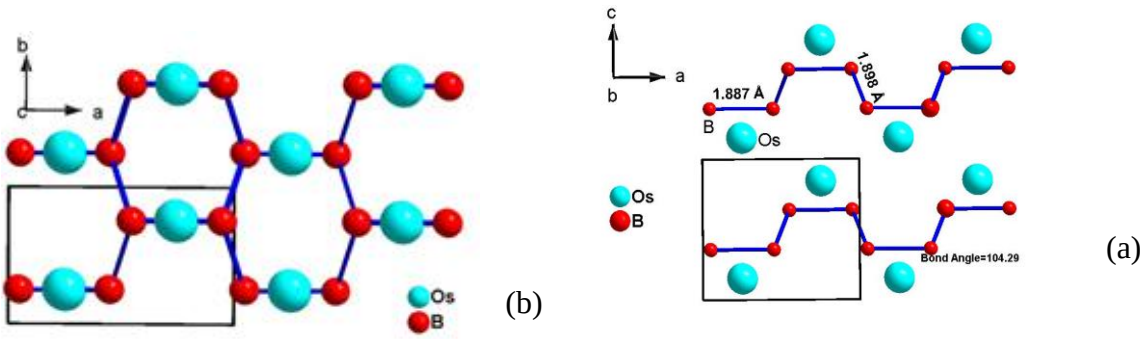

Figure 3.6 The crystal structure of OsB_2 constructed using information obtained from XRD pattern.

Figure 3.6 (a) shows the OsB_2 structure when viewed along the c-axis and (b) shows the structure when viewed perpendicular to the c-axis. Along the c-axis boron layers lie between two planar layers of osmium atoms which are offset along the ab plane [17]. Compared to the MgB_2 structure which also has alternate planes of boron and magnesium atoms stacked along c-axis.

3.3 Superconducting Properties

The resistivity (ρ) versus temperature (T) measurements were carried out on the OsB_2, RuB_2, and $LuRuB_2$ samples in the PPMS using four probe method. The plots of ρ vs T are shown below.

OsB_2 and RuB_2: The ρ vs T data for OsB_2 are shown in Fig. 3.7. The data are similar to the published results. The inset in Fig. 3.7 shows a sharp superconducting transition with a Tc = 2.1 K consistent with previous results. This confirms the good quality of our sample. Pressure dependence of the Tc for OsB_2 will be discussed later.

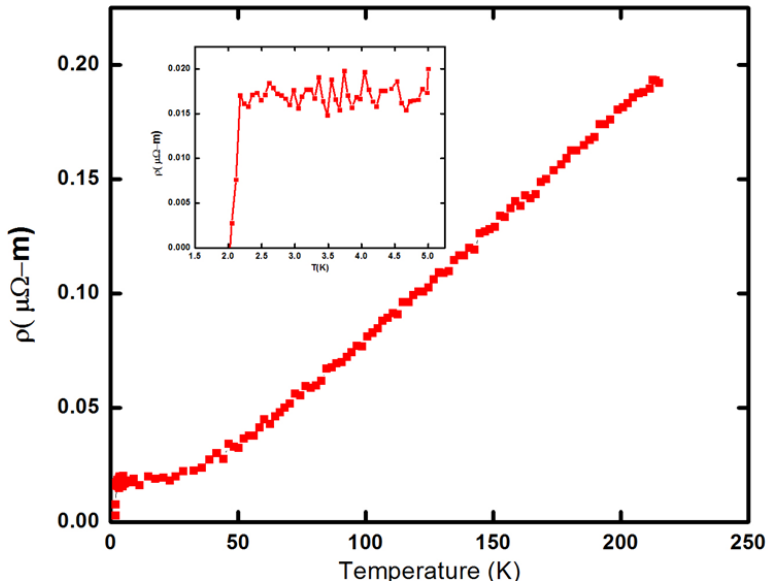

Figure 3.7 Electrical resistivity versus temperature for OsB_2. The inset shows the low temperature data on an expanded scale to highlight the transition characteristic of superconductors.

The ρ vs T data for RuB_2 are shown in Fig. 3.8. RuB_2 and OsB_2 show metallic behavior with approximately linear decrease in resistivity on cooling. At low temperatures, ρ is only weakly temperature dependent. RuB_2 reaches a residual resistivity ρ_0 of 1.59 μΩ-cm at around 2 K The residual resistivity ratio (RRR), defined as ρ(300 K)/ ρ_0 is 18.7 for RuB_2. The RRR varies strongly for a material depending on the amount of impurities and other crystallographic defects. So it is used as an indicator of the purity and overall quality of a sample. Since resistivity usually increases with increase in defects, a large RRR indicates well crystallized homogenous samples. The large value of RRR = 19 for RuB_2 confirms the good quality of our sample. At the lowest temperatures T ~ 0.4 K, even for the smallest excitation current I = 0.1 mA, we observed heating effect while measuring electrical resistivity for RuB_2. This did not allow us to measure the low temperature superconducting properties properly. Even so, we observed a superconducting transition for RuB_2. The inset in Fig. 3.8 shows a sharp superconducting transition with a zero resistance at Tc = 1.5 K.

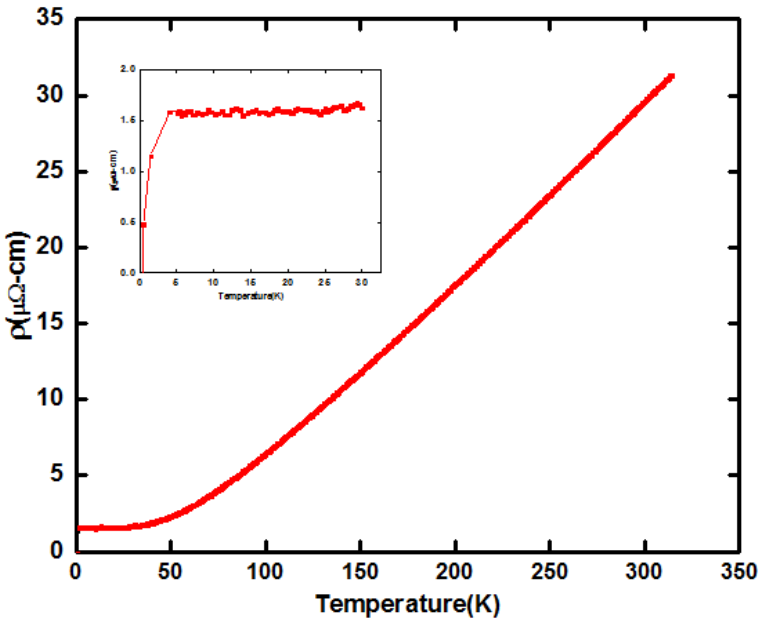

Figure 3.8 Electrical resistivity versus temperature for RuB_2. The inset shows the low temperature data on an expanded scale with a transition around 1.5 K.

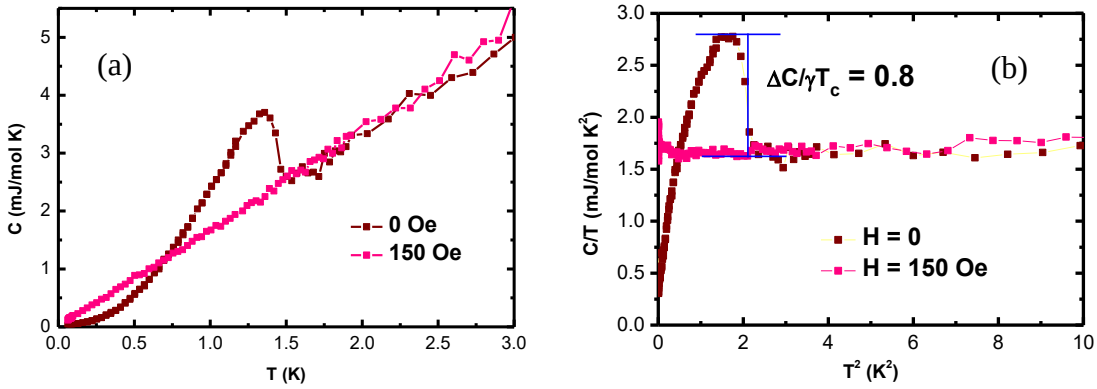

Figure 3.9 (a) Heat Capacity C for RuB_2 in applied fields H = 0 Oe and 150 Oe. (b) C/T versus T^2 for RuB_2 in applied fields H = 0 Oe and 150 Oe.

Heat capacity measurements were also carried out on RuB_2 as shown in Figure 3.9(a) and (b). The transition in zero field is quite sharp. This confirms bulk superconductivity. In an applied field of 150 Oe, no superconducting transition is seen down to 60 mK. This suggests that the critical field for RuB_2 is less than or equal to 150 Oe. So RuB_2 is a small critical field

superconductor compared to other superconductors like OsB_2 which has been reported to have critical fields of up to 420 Oe. The jump in the specific heat at the superconducting transition is normalized as $\Delta C/\gamma T_c$, where γ is the Sommerfeld coefficient. $\Delta C/T_c$ is estimated from Figure 3.9 (b) and has been found to be approximately 1.24 mJ/mol K^2. γ is found from the intercept in Figure 3.9 (b) as approximately 1.62 mJ/mol K^2. Thus, $\Delta C/\gamma T_c$ is approximately 0.8. This is significantly smaller than the value 1.43 expected from the BCS theory. A similar reduced value of $\Delta C/T_c$ has been observed earlier for the multi-gap superconductors MgB_2 and OsB_2. The origin of the reduced value for RuB_2 might also lie in the multi-gap nature of its superconductivity although further measurements are needed to test this hypothesis. Due to the low critical temperatures of OsB_2 and RuB_2 at 0 Tesla alone, it was difficult to detect the suppressed critical temperatures on applying magnetic field.

LuRuB$_2$: The r vs T data for $LuRuB_2$ are shown in Fig. 3.10. The resistivity values at room temperature (300 K) is 29.2 μΩ-cm for $LuRuB_2$. $LuRuB_2$ reaches a residual resistivity ρ_0 of 10.24 μΩ-cm at around 11.8 K. The residual resistivity ratio (RRR), defined as $\rho(300\ K)/\ \rho_0$ is 2.85 for $LuRuB_2$. This value is quite small and probably reflects the fact that the LuRuB2 sample has many defects. This is consistent with the large amounts of secondary phases observed in the powder x-ray diffraction for this sample.

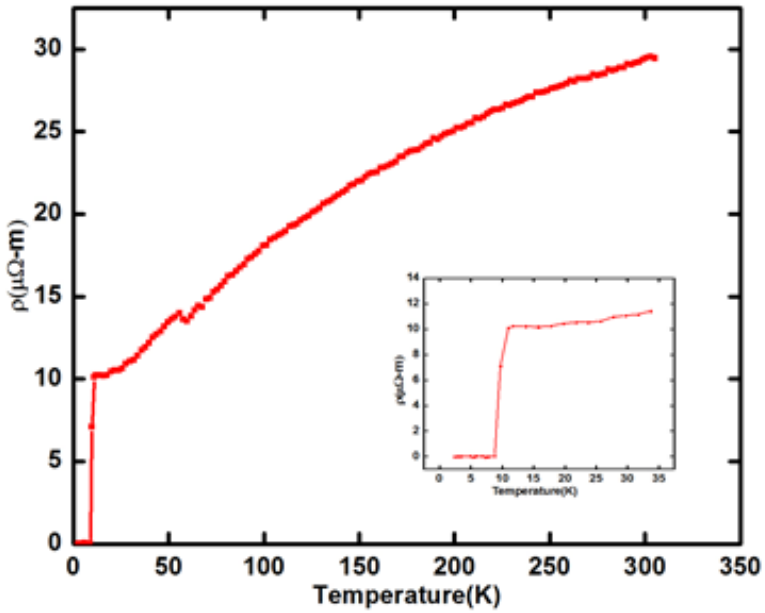

Figure 3.10 Electrical resistivity versus temperature for $LuRuB_2$. The inset shows the low temperature data on an expanded scale with a transition around 10.98 K.

Our goal in this study was to investigate the H-T and P-T phase diagrams of the superconducting phase in $LuRuB_2$. We believe that the presence of the secondary phases, all of them being non-magnetic and non-superconducting above 2 K does not affect our primary goal.

The inset in Fig. 3.10 shows that ρ drops abruptly to zero below the superconducting critical temperature Tc =9.8 K. This is consistent with an earlier report. In order to study the dependence of critical temperature with applied external field, the resistivity measurements were carried out on $LuRuB_2$ at different fields. In Fig. 3.11 we show the low temperature ρ vs T measured at various applied magnetic fields H. We can track the suppression of Tc with H and construct an H-T phase diagram.

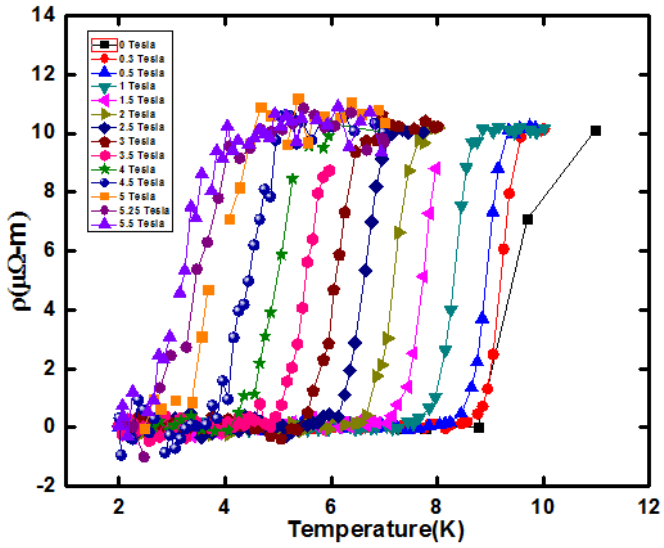

Figure 3.11 Suppression of critical temperature of $LuRuB_2$ with increasing applied magnetic field

Such an H-T phase diagram has been constructed for LuRuB2 and is shown as the red symbols in Fig. 3.12. We find an anomalous linear dependence of the critical field on T. This behavior

is not consistent with the predictions of the BCS theory as shown by the blue curve in Fig. 3.12.

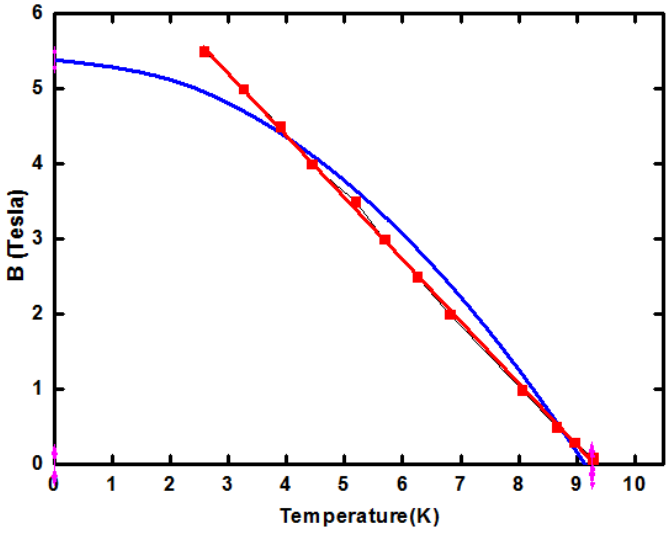

Figure 3.12 Red line shows critical temperature of $LuRuB_2$ at different applied magnetic fields. Blue curve represents the behavior expected in a conventional BCS superconductor.

This deviation from the expected curve could suggest that $LuRuB_2$ is probably an unconventional superconductor though the exact mechanisms have to be studied. The critical field is found to be 7.6 Tesla and critical temperature is 9.309 K (Figure 3.12).

3.3 Pressure dependence of Superconductivity

The effect of pressure on these superconductors was also studied by placing them in a pressure cell. Since lead and tin are easily available in high purity, they have extremely sharp superconducting transition. The suppression in the T_c of lead was used in order to find how much pressure was applied at low temperatures. Lead has been calibrated to have dT_c/dP = -0.386 K/GPa.

Fig.3.13 shows the magnetization (m) vs T for OsB_2 at ambient and 1 GPa pressure. The inset in Fig. 3.13 shows that the Tc for OsB_2 shifts to lower temperatures with pressure.

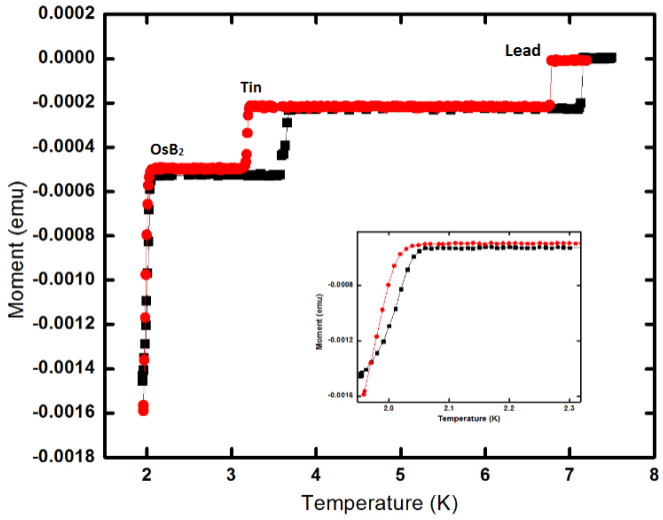

Figure 3.13 Pressure measurement for OsB_2. The black curve shows moment vs temperature at zero pressure and the red curve shows moment vs temperature at a pressure of about 1 kbar. The inset shows low temperature transition for OsB_2 on an expanded scale.

Fig. 3.14 shows the m vs T measurements at various pressures P for LuRuB2 to study the dependence of superconducting Tc on P. The lower temperature superconducting transition is of Pb. The P-T phase diagram was extracted from these data and is shown in Fig, 3.15. Tc is suppressed approximately linearly with pressure at a rate of dTc/dP = -0.27K/GPa.

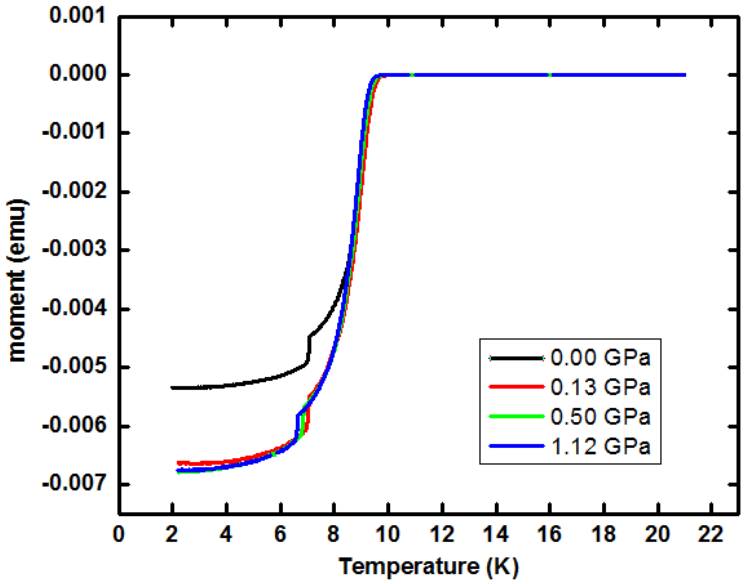

Figure 3.14 Change in critical temperature of $LuRuB_2$ with pressure. Black curve is without pressure, red curve at intermediate pressure and blue curve at maximum pressure. The transition seen at around 7 K is due to lead while that at around 10 K is for $LuRuB_2$.

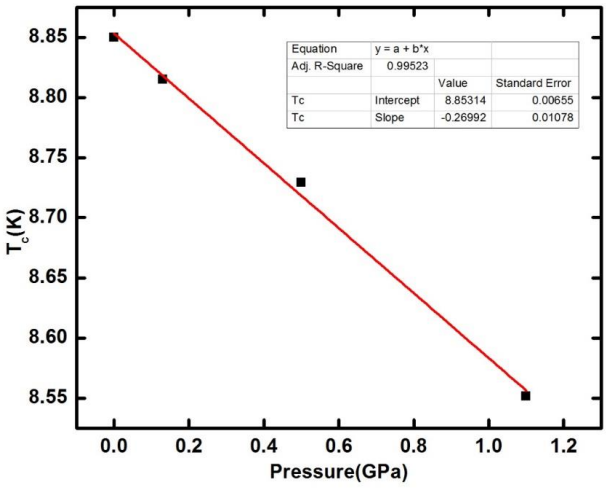

Figure 3.15 The critical temperature of $LuRuB_2$ falls with pressure. dT_c/dP is found to -0.2699 K/GPa

Most of the superconductor exhibit lattice instabilities. Applying external pressure to these superconductors can cause the lattice instabilities to increase or decrease. This is due to the variation in the principal parameters determining the superconducting properties such as the electronic density of states at the Fermi energy, $N(E_F)$, the characteristic phonon frequency, and the coupling constant of electrons and phonons. Thus external pressure can be used to tune the T_c and the superconducting properties. Almost all of the superconductors exhibit a decrease of T_c with pressure. This has been attributed to the volume dependence of $N(E_F)$ and of the effective interaction between the electrons due to the electron-phonon coupling [18]. Pressure-induced changes of the Fermi surface topology has also been reported to be the cause of change in critical temperature of some compounds [19, 20]. Thus, in order to estimate T_c as a function of imposed pressure, we need to know the pressure dependence of its microscopic parameters like the average phonon frequency, ω_D, the electronic density of states, $N(E_F)$, etc.

According to the weak-coupling BCS theory Tc is given by

$$k_B T_c = 1.13\hbar\omega_D \exp\{-1/\lambda\} \qquad (22)$$

k_B and ħ are Boltzmann's and Planck's constant, respectively, $\lambda = N(E_F)V_{eff}$, and V_{eff} is the effective interaction between the electrons mediated by the electron-phonon coupling. The phonon frequency usually increases with pressure due to phonon hardening. So the observed decrease of T_c with pressure must be due to a decrease of λ. The average value of the electronic density of states is expected to decrease under pressure because of the pressure-induced band broadening effect. The pressure dependence of V_{eff} is more difficult to estimate [21]. By applying pressure on OsB_2, it was hoped that a structural transition would take place and that the boron layers in the compound would become flat. This would make OsB_2 structurally very similar to MgB_2 and thus an increase in T_c was expected. However, the pressure applied was not enough to cause structural deformation and thus the other factors mentioned above probably caused a decrease in T_c.

3.2 Conclusion and Future Work

Measurements on crystals OsB_2, RuB_2 and $LuRuB_2$ confirm bulk superconductivity. Pressure studies revealed that the critical temperature of these compounds decrease with increasing pressure. The dependence of critical temperature with applied external magnetic field was also studied. Further studies have to be carried out in order to gain deeper understanding of the multigap nature of superconductivity of these samples. Growth of single crystals of these compounds would greatly facilitate the study of anisotropic properties. The linear dependence of critical temperature with applied field seen in $LuRuB_2$ is quite unusual even for an unconventional superconductor. However the sample of $LuRuB_2$ contained several other phases as well. This unusual behavior could be a result of the differential lattice strain experienced by the phase impure sample. The studies have to be repeated on a single phase sample of $LuRuB_2$ before any conclusive results can be found.

Bibliography

[1] McCusker, L. B., Von Dreele, R. B., Cox, D. E., Louër, D. & Scardi, P. (1999). *J. Appl. Cryst.* **32**, 36–50.Brian

[2] H. Toby (2006). R factors in Rietveld analysis: How good is good enough?. Powder Diffraction, 21, pp 67-70. doi:10.1154/1.2179804.

[3] Vibrating Sample Magnetometer (VSM) Option User's Manual, Quantum Design

[4] High Pressure Cell User Manual For use with the QD MPMS, PPMS VSM, and VersaLab VSM systems

[5] A. A. Golubov et al., J. Phys. Condens. Matter 14, 1353 (2002).

[6] H. J. Choi et al., Nature (London) 418, 758 (2002).

[7] M. Iavarone et al., Phys. Rev. Lett. 89, 187002 (2002).

[8] G. Rubio-Bollinger, H. Suderow, and S. Vieira, Phys. Rev. Lett. 86, 5582-5584 (2001).

[9] M. R. Eskildsen et al., Phys. Rev. Lett. 89, 187003 (2002).

[10] J. Nagamatsu et al., Nature 410, 63 (2001).

[11] H. J. Choi et al., Nature (London) 418, 758 (2002)

[12] H. Suhl, B. T. Matthias, L. T. Walker, Phys. Rev. Lett. 3, 552 (1959).

[13] V. Z. Kresin and S. A. Wolf, Physica C 169, 476 (1990).

[14] D. Kaczorowski, A. J. Zaleski, O. J. Zogal, and J. Klamut, cond-mat/0103571.

[15] V. A. Gasparov, N. S. Sidorov, I. I. Zverkova, and M. P. Kulakov, JETP Lett. 73, 532 (2001).

[16] H. Rosner,W. E. Pickett, S.-L. Drechsler, A. Handstein, G. Behr, G. Fuchs, K. Nenkov, K.-H. Muller, and H. Eschrig, Phys. Rev. B 64, 144516 (2001).

[17] Y. Maeno, T. M. Rice, and M. Sigrist, Phys. Today 54,42 (2001)

[18] L. D. Jennings and C. A. Swenson, Phys. Rev. 112, 31 (1958).

[19] J. Hatton, Phys. Rev. 103, 1167 (1956).

[20] C. W. Chu, T. F. Smith, and W. E. Gardner, Phys. Rev. Letters 20, 198 (1968).

[21] 0B. Lorenz and C. W. Chu, in Frontiers in Superconducting Materials, edited by A. V. Narlikar Springer, Berlin, 2005, p. 459.

[22] Y. Singh, A. Niazi, M. D. Vannette, R. Prozorov, and D. C. Johnston, Phys. Rev. B 76, 214510 (2007)

[23] Y. Singh, C. Martin, S. L. Bud'ko, A. Ellern, R. Prozorov, and D. C. Johnston, ibid. 82, 144532 (2010)

[24] Robert C Richardson, Eric N. Smith, Experimental Techniques in Condensed Matter Physics at Low Temperatures